Additive Manufacturing 84 (2024) 104113

Contents lists available at ScienceDirect

Additive Manufacturing

journal homepage: www.elsevier.com/locate/addma

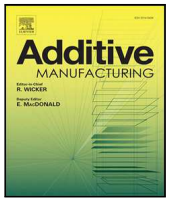

Research paper

Rethinking ductility—A study into the size-affected fracture of additively manufactured polymers

Zainab S. Patel [a], Abdulaziz O. Alrashed [b], Kush Dwivedi [b], Marco Salviato [c], Lucas R. Meza [b,*]

[a] Materials Science and Engineering, University of Washington, Seattle, WA, 98195, United States of America
[b] Mechanical Engineering, University of Washington, Seattle, WA, 98195, United States of America
[c] Aeronautics and Astronautics, University of Washington, Seattle, WA, 98195, United States of America

ARTICLE INFO

Keywords:
Small-scale fracture
Size effect law
Ductile-to-brittle
Two-photon lithography

ABSTRACT

Ductility, namely a material's capacity for plastic deformation, is a key property for preventing fracture-driven failure in engineering parts. While some brittle materials are known to exhibit ductility at small scales, the underlying mechanics of such behaviors are not well understood. This work identifies size-affected fracture as a key mechanism for the origin of ductility in two-photon lithography (TPL) fabricated polymers. We conducted microscale single-edge notch bend (μSENB) fracture experiments on three distinct specimen sizes and varied the polymer degree of conversion (DC) to be between 17% and 80% by controlling both laser exposure and post-write thermal annealing. For a given specimen size, we find that shifting from low to high DC predictably causes a ~3x and ~4x increase in strength and bending stiffness, respectively, but the fracture energy correspondingly drops by ~6x, from 180 J/m^2 to 30 J/m^2. Notably, this reduced fracture energy was accompanied by a ductile-to-brittle transition (DBT) in the failure behavior. Using a combination of experiments and finite element analysis, we quantify the fracture yielding zone size (r_p) in these polymers as a function of DC and demonstrate that ductility emerges when r_p approaches the sample width irrespective of the DC. This finding provides a crucial insight that ductility is a size-induced property that occurs when features are reduced below a characteristic fracture length scale and that strength, stiffness, and toughness alone are insufficient predictors of ductility.

1. Introduction

Bend, do not break—materials capable of sustaining deformation without failure are crucial to advanced technologies from semiconductors to aerospace. A material's mechanical resilience depends on its toughness, namely the amount of energy that it dissipates prior to failure. Much of this energy dissipation comes from intrinsic mechanisms like plasticity and internal friction. While materials are often categorized as being ductile or brittle, all materials have energy dissipation mechanisms that occur at some length scale [1–3]. This may be at the centimeter scale, e.g. for metals, or at the nanoscale, e.g. for ceramics. Understanding the interplay between ductility and the length scale of energy dissipation mechanisms is crucial to creating new materials with enhanced toughness.

Ductility itself quantifies the extent of plastic deformation in a material prior to fracture. Materials with highly active plasticity mechanisms like dislocations in metals or chain sliding in polymers are thought to be more ductile, and processing methods correctly focus on activating these mechanisms to promote ductility [4–8]. Ongoing efforts in nanomechanical materials testing has demonstrated a unique phenomenon of size-enhanced ductility, and there are numerous experimental and computational studies showing that ductility emerges at small scales in materials that are otherwise considered to be brittle, such as silicon [9–11], amorphous carbon [12–14], metallic glass [15] and even quasicrystals [16]. This size-enhanced ductility is generally attributed to modified stress states at small scales or the activation of new plasticity mechanisms, but the true mechanistic origins of ductility remained unclear.

Ascertaining the origins of ductility first requires an understanding of fracture processes. Prior to fracture, materials will develop a yielding zone of length r_p in front of a crack, which comprises a fracture process zone (FPZ) of length l_{ch} and a plastic zone (PZ) of effective length r_p-l_{ch}. Samples larger than this yielding zone will undergo fracture-governed failure, while samples smaller than this yielding zone will undergo strength-driven failure. In the strength-driven regime, materials with a large PZ and small FPZ will experience ductile fracture,

* Corresponding author.
E-mail address: lmeza@uw.edu (L.R. Meza).

https://doi.org/10.1016/j.addma.2024.104113
Received 16 November 2023; Received in revised form 26 February 2024; Accepted 2 April 2024
Available online 4 April 2024

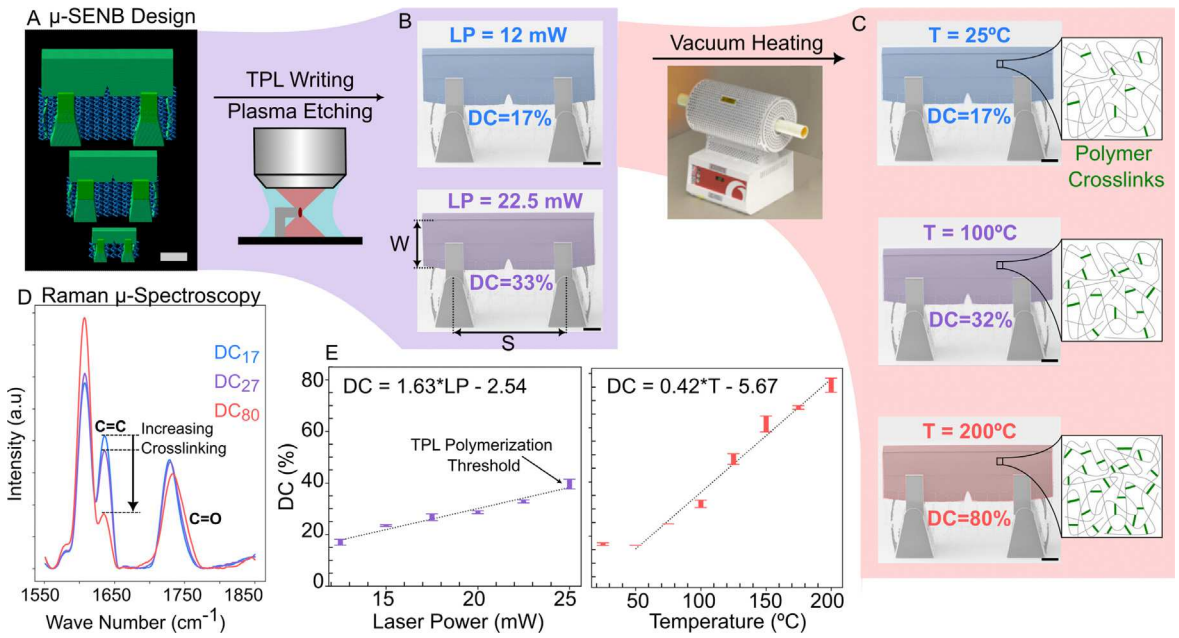

Fig. 1. Polymer Degree of Conversion (*DC*): (A) Graphic rendering of the μSENB design showing the three different beam sizes tested in this study. (B) Specimens with *DC* values between 17%–39% generated using different laser exposures in TPL. (C) Specimens with starting *DC* value = 17% are heated under vacuum to generate specimens with *DC* values between 17%–80%. Insets illustrate increasing cross-linking density. (D) Raman spectra for specimens with three different *DC* values showing the decreasing intensity of the C=C peak, which correlates to increased cross-linking between the polymeric chains. (E) Raman data showing the effect of laser power and temperature on *DC*. All scale bars = 10 μm.

while materials with a small PZ and large FPZ will experience quasi-brittle fracture. Many studies in this field, pioneered by Bažant, have explored the size-affected transition from fracture-driven to strength-driven failure [17–20], but they often focus on the nominal strength in quasi-brittle materials like concrete and rock and ignore emergent small-scale ductility.

Two-photon lithography direct laser writing (TPL-DLW) provides an ideal platform for studying size-affected fracture due to its exceptional ability to create parts with feature sizes as small as 100 nm [21,22]. It has been highly successful in creating metamaterials with novel mechanical performance in part because it enables the utilization of size-enhanced nanomaterial properties [23–26]. Significant work has gone toward understanding the role of process parameters on TPL polymer performance, particularly the relationship between the degree of conversion (*DC*) – i.e., the extent of cross-linking between polymer chains – and strength and stiffness [27,28]. While these properties are important, there is currently a lack of information on how TPL process parameters and the resulting characteristic length scales affect fracture performance.

In this study, we use microscale single-edge notch bend (μSENB) experiments to investigate the strength, stiffness, toughness, and ductility of a TPL-DLW polymer as a function of *DC* and part size. Experiments reveal that increasing the *DC* from 17% to 80% increases both strength and bending stiffness by a factor of ~3× and ~4×, respectively, but that there is a corresponding ~6× reduction in the toughness that additionally coincides with a ductile-to-brittle transition (DBT) in the polymer. To understand this DBT, we conduct size-effect experiments and develop an elastic–plastic-damage finite element (FE) model with properties fit to the experimental strength and toughness data. We then demonstrate how changes in both sample size and yielding zone size induce size-affected changes in fracture behavior.

2. Sample preparation and characterization

2.1. Design

Microscale beams with varying degrees of conversion were designed in a single-edge notch bend (μSENB) configuration. Beam dimensions were determined according to ASTM E-1820b [29] with a standard beam thickness of W = 26 μm and span-to-thickness ratio S/W = 2. Notches were directly written into the beams during the printing process to avoid introducing any focused ion beam (FIB) milling damage [1]; these had an initial length a_o = 4.5 μm and an a/W = 0.17. Additional geometrically scaled specimens with thicknesses equal to W, 2W/3, and W/3 were created to characterize the size of the fracture yielding zone and the material fracture energy.

Two separate variables were used to change the polymer degree of conversion: (i) laser power (LP) was varied between 11 mW to 25 mW in ~2.5 mW increments, and (ii) annealing temperature (T) was varied between 25 °C to 200 °C in ~25 °C intervals (Figs. 1A, B, C and S1). The maximum temperature of 200 °C was chosen because it is well below the degradation onset temperature of the photopolymer of ~250 °C [28]. Using temperature as a control variable not only allows samples to have a higher *DC* than what can be achieved with TPL alone, but it creates an overall more homogeneous material with a uniform degree of conversion through the cross-section. This minimizes any additional toughening due to material heterogeneity effects [30].

2.2. Fabrication

Specimens were fabricated on silicon substrates, which were first etched for 5 minutes in oxygen plasma (Plasma Etch PE25) and then functionalized using 3-(Trimethoxysilyl) propyl methacrylate to improve adhesion and prevent peeling off of supports during fracture tests. Printing was done using a two-photon lithography (TPL) direct laser writing (DLW) system (Nanoscribe, GmbH). A proprietary acrylate-based resist, IP-Dip (Nanoscribe, GmbH), was used with a 63× objective to achieve high-precision, sub-micron resolution writes. Writing speeds, specimen hatching, and layering were all kept constant at 10 mm/s, 100 nm, and 300 nm, respectively, to minimize any heterogeneity from the TPL-DLW process. Support lattices were written in piezo mode with a low laser power (6 mW) to ensure faster etching. After printing, samples were immersed in a propylene glycol monomethyl ether acetate (PGMEA) solution for 20 mins, then in ultrapure IPA for 30 mins, followed by critical point drying (Tousimis Autosamdri-931). These were subsequently etched in an oxygen plasma etcher (YES

CV200 RFS) at 65 W power for 25–35 mins until the support lattices were completely removed, producing free-standing fracture specimens, a method first demonstrated by Gross et al. [31]. Thermal treatment samples were written with a 15 mW laser power, then heated in a high vacuum tube furnace (Carbolite Gero), and maintained at their peak temperature for 1 hour. Large sweeps were written to quantify the polymer degree of conversion as a function of laser power and temperature (Fig. S1).

2.3. Raman micro-spectroscopy

Raman micro-spectroscopy was performed on printed beam samples to quantify their DC. Raman Spectra were acquired using an inVia (Renishaw plc) confocal Raman microscope with a 50× objective, operated at an excitation wavelength of 785 nm, with a laser intensity of 50% and an exposure time of 10 s averaged over 3 acquisitions. DC values were extrapolated from Raman spectra using the relationship $DC = 1-(\frac{A_{C=C}/A_{C=C}}{A'_{C=C}/A'_{C=C}})$ [32]. Here, $A_{C=C}$ and $A_{C=C}$ are the integrated intensities of the carbon–carbon and carbon-oxygen double bond peaks in the polymerized resin, respectively, and $A'_{C=C}$ and $A'_{C=C}$ are the integrated intensities of the same peaks in the unpolymerized resin.

Raman spectra revealed that DC increases linearly with both laser power and temperature as $DC = 1.629 * LP - 2.54$ and $DC = 0.418 * T - 5.67$, respectively (Figs. 1D, E and S2). Varying the laser power produced DC values between 17%–40%, with 40%–45% being the upper limit that can be achieved without overexposing the resin. Heating of samples printed with $DC = 25\%$ had no effect up to 50 °C, after which the DC linearly increased to a maximum of 80% at 200 °C. The mechanical properties of this resin system can be estimated based on literature data for both as-written samples [27] and for fully cross-linked samples [28], which show Young's modulus and yield strength variation between 1.5–4.3 GPa and 30–80 MPa, respectively, for the range of DC studied here.

2.4. Nanomechanical testing

Displacement-controlled in-situ μSENB fracture tests with continuous stiffness measurement (CSM) were conducted using a piezo-driven nanoindentation system (ASA, Alemnis AG). Testing was done in a scanning electron microscope (SEM) (Thermo-Fisher Scientific Apreo) with a 2 μm radius conductive diamond wedge tip. Quasistatic tests were conducted with a loading rate of 20 nm/s, and specimens were tested either to complete fracture or to a displacement of 18 μm. Video data were captured for each test. We note that for the purposes of this study, any strain rate-dependent behavior is ignored. A sinusoidal signal of amplitude 40 nm and frequency 4 Hz was superimposed to perform continuous stiffness measurement (CSM) and thereafter compute instantaneous crack lengths. To account for thermal drift, the nanoindenter assembly was installed in the SEM and allowed to stabilize before testing. We additionally added 'out-of-contact' segments before and after the compression step where the tip is not in contact with the sample to correct for any drift in the system. Thermal drift showed a linear correlation with time for short experiment times (less than 30 minutes) and was subsequently subtracted from the load data during data processing. An amplitude-based Fast Fourier Transform (FFT) noise filtering algorithm was used to remove noise from the load–displacement data. Subsequent CSM Data was smoothed using the Savitzky–Golay filter by fitting a third-order polynomial for every 300–400 data points.

2.5. J-R curve calculation

Instantaneous load line stiffness was calculated using the unloading slope of the CSM data, and crack initiation was determined as the point where the unloading stiffness began to decrease. Crack lengths were obtained using a compliance calibration procedure [33] by correlating the crack initiation point with the instantaneous stiffness thereafter. An elastic–plastic Mode-I J-integral was used to determine the samples' fracture behavior and crack growth resistance as defined in ASTM E1820-20b [29]. In softer samples, a critical J-integral value could not be computed using traditional EPFM methods since the J-R curves did not plateau. We, therefore, define a conditional J_Q value to be the J-integral value at a crack extension of $\Delta a = 2$ μm. It should be noted that this J_Q value is a severe underestimation of the true fracture energy for these materials. In samples that show brittle behavior and fail catastrophically, J_Q was calculated at the point of maximum load.

2.6. Computational framework

To account for the significant plasticity and post-failure strain softening exhibited by the TPL polymers, an elastic–plastic-damage model was adopted from Salviato [34] and implemented as a VUMAT subroutine in ABAQUS/Explicit with C3D8R mesh elements. Beams were modeled to be homogeneous, i.e., without any cross-linking gradients,

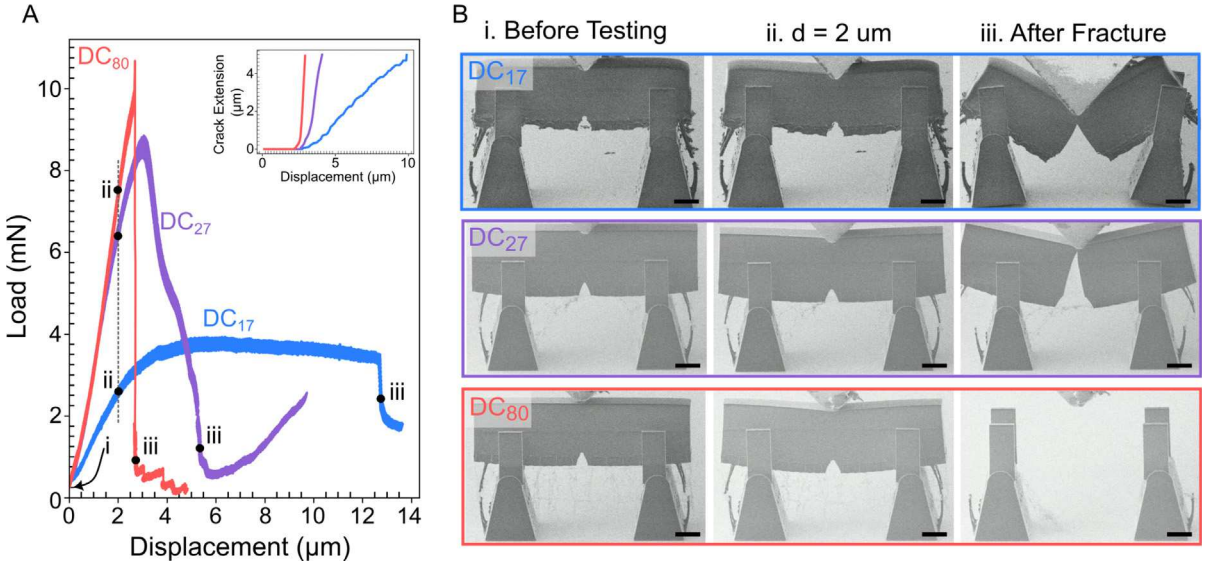

Fig. 2. Mechanical Testing Results: (A) Representative load–displacement curves for samples with DC_{low}, DC_{med}, and DC_{high} with inset showing corresponding crack extension vs. displacement. Hollow circles represent the point of crack initiation. (B) SEM stills from in-situ videos showing the different failure behaviors observed. Scale bar = 10 μm.

because the in-plane hatching and out-of-plane layering distances between the voxels were sufficiently smaller than the size of the voxel. Sharp cracks, with a crack tip radius comparable to the size in the fabricated beams (~ 250 nm), were used, and it was assumed that the cracks would propagate in a self-similar manner. The support structures and the indenter tip were modeled as elastic materials with an elastic modulus and Poisson's ratio of 3.5 GPa, 0.35, and 200 GPa, 0.33, respectively. A frictional penalty contact was defined between the beam and supports, as well as between the beam and the indenter tip. Materials were taken to be elastic-linear hardening with a tension/compression strength asymmetry and damage evolution as a function of equivalent plastic strain using a crack band model [35,36]. Material properties were first estimated using uniaxial tension and compression data from Bauer et al. [27,28] and then refined to fit experimental data in this work. The elastic modulus, yield strength, and plastic stress–strain properties were obtained from bend tests on unnotched beams, while the fracture energy was determined from experiments on notched beams (Fig. S5).

3. Stiffness, strength and fracture energy

The mechanical response of the different test specimens was found to correlate strongly with the *DC* regardless of whether samples were tested in an as-written state or were thermally annealed. The peak load and bending stiffness both increased with *DC*, ranging from 4 mN to 11 mN and 1.2 kN/m to 4.3 kN/m, respectively. There was little variation in strength or stiffness after $DC \approx 40\%$, but specimens with a higher *DC* showed significantly lower strains to failure. Representative load–displacement data are shown in Fig. 2, and the complete data set for all samples tested is provided in Fig. S3.

We observed three characteristic deformation regimes depending on the *DC* value, which we will distinguish here as DC_{low} for values between 17%–25%, DC_{med} for values between 25%–40%, and DC_{high} for values greater than 40%. Beams with DC_{low} showed elastic–plastic behavior with long plastic plateaus and slow, stable crack propagation. In DC_{med} specimens, the mechanical behavior was linear up to peak load, followed by gradual softening and stable crack propagation. In contrast, all DC_{high} specimens showed a linear-elastic behavior up to the peak load, followed by unstable crack propagation and catastrophic failure. Stills from in-situ videos are shown in Fig. 2, demonstrating the significant change in failure behavior with increasing *DC* (see Supplementary Movies S1–S3).

The load–displacement and CSM data were further analyzed to quantify the fracture properties, details of which can be found in 2.5. Three distinct J-R crack resistance behaviors were observed across the range of *DC* values studied, as shown in Fig. 3. In the DC_{low} samples, the moderate softening after the peak load resulted in stable crack propagation and rising J-R curves, with fracture energies as high as $J_Q = 180$ J/m^2, where J_Q is the J value at 2 μm of crack extension. In samples with DC_{med}, the greater post-yield softening caused a faster crack propagation, resulting in lower fracture energies of J_Q = 40–60 J/m^2. The lower J-R curve slope and near plateau in the J value of the DC_{med} samples indicate that they have a nearly fully developed yielding zone. For samples with DC_{high}, crack growth was unstable, and they had correspondingly lower fracture energies of $J_Q = 30$ J/m^2.

This pronounced ~6× reduction in J_Q between *DC* = 17% and *DC* = 80% specimens is shown in Fig. 3. Although thermal treatment has been proposed as a homogenization method to eliminate part-to-part property variation and maximize performance [28], these results illustrate that the enhanced strength and stiffness from thermal treatment comes at a significant cost of toughness. The IP-Dip material has a trade-off between strength and toughness, namely toughness decreases as strength increases [37]. An optimal balance between strength and toughness can be obtained for samples with a *DC* in the range of 20%–25%, an important consideration for fabricating parts for structural purposes. Note that the J_Q values here should not be considered true material properties for any test where the J-R curve did not plateau, but they do represent meaningful trends in material properties.

The large drop in fracture energy with increasing *DC* in this work matches well with existing models for polymer fracture energy, which is known to depend strongly on the proportions of cross-linked and entangled chains [38]. Materials with high chain cross-linking density tend to experience brittle failure via chain scission, while those with high chain entanglement density undergo ductile failure via chain sliding [39–41]. Various models have been developed to assess the impact of network architecture and defects on fracture energy (G_t) [38,42,43], which find that fracture energy scales inversely with chain cross-linking density (v_x) as $G_t \propto v_x^{-1/2}$ in highly elastic materials and $G_t \propto v_x^{-4}$ in elastic–plastic materials [41]. In both cases, lower cross-linking density leads to greater energy dissipation and a corresponding enhanced toughness. However, despite attempts to connect this fracture energy to characteristic length scales [41,44], there is no mechanistic explanation for the observed ductile to brittle transitions in this or other work.

4. Ductile-to-brittle fracture transition

Ductile-to-brittle transitions are well known to occur in various crystalline and amorphous polymers [6,44,45]. These transitions have

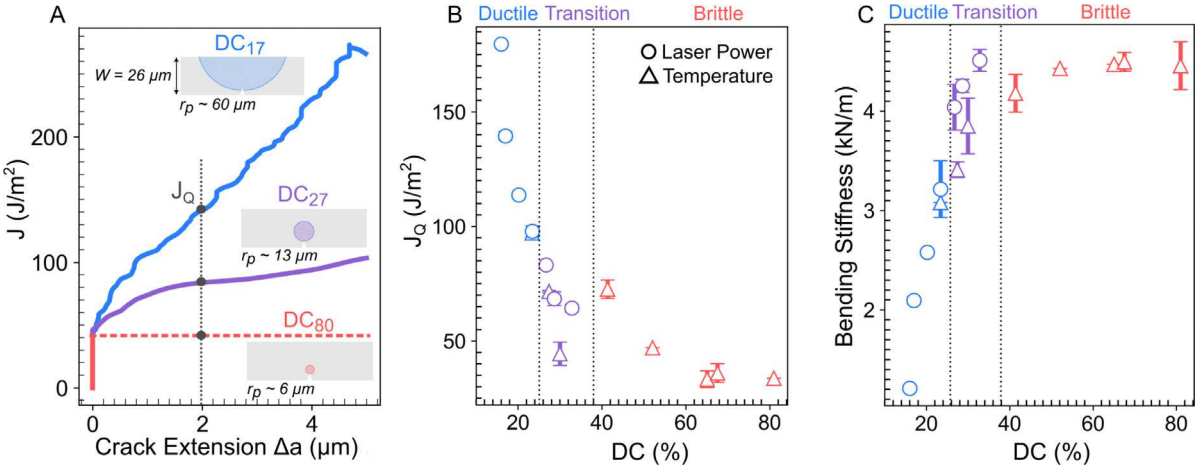

Fig. 3. J-R curves, Fracture Energy and Bending Stiffness: (A) Representative J-R curves showing decreasing crack growth resistance with increasing *DC*. Insets show plastic zone sizes of respective materials. (B) Fracture Energy and vs. *DC* for all samples tested in this study, showing decreasing fracture energy with increasing DC. (C) Bending stiffness vs *DC* for all samples tested in this study, showing increasing sample stiffness with DC. Error bars represent standard deviation values from at least three runs on each specimen type.

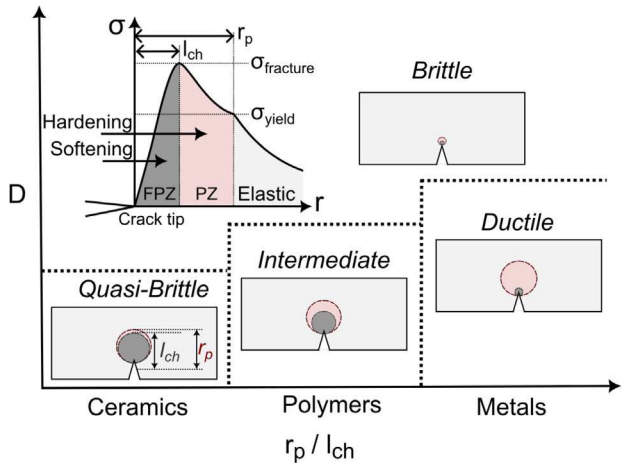

Fig. 4. Fracture Transitions Changing fracture behavior with changing sample size (D) w.r.t to the relative size of the sample yielding zone (r_p) and fracture process zone (l_{ch}).

been connected to external factors such as temperature and loading rate and internal factors like molecular weight, density, and microstructure [44]. One essential aspect of these transitions is the ratio of sample size (D) to characteristic fracture length scales. Prior to fracture, a yielding zone of size r_p will develop in front of a flaw. This encompasses a fracture process zone (FPZ) of size l_{ch}, i.e., a damage-driven softening zone at the crack tip, and a plastic zone (PZ) of size (r_p–l_{ch}), i.e., a plastic hardening zone around the FPZ. Standards for measuring fracture toughness generally require specimens to be significantly larger than these fracture length scales (i.e., $D \gg r_p$) to ensure a small-scale yielding condition [29]. In these scenarios, samples will form a small plastic region at the tip of a crack while the rest of the sample remains linear elastic, and brittle failure – i.e., unstable crack growth – will occur when a crack or flaw reaches a critical size.

Small samples with $D \leq r_p$ generally have an enhanced ductility due to energetic size-effects, namely when there is insufficient fracture energy to cause unstable crack growth according to linear elastic fracture mechanics (LEFM). When the PZ is much larger than the FPZ (i.e., $l_{ch} \ll r_p$), as is the case for many metals, materials will exhibit an increasingly ductile response due to large scale yielding as D is decreased [46]. When the FPZ is much larger than the PZ (i.e., $l_{ch} \approx r_p$), materials will show a quasi-brittle response wherein a large damage zone will develop that suppresses crack propagation, as is the case for most ceramics [18], concrete [17] and polymer nanocomposites [47]. An understanding of ductile-to-brittle transitions is currently lacking for polymeric material systems where both PZ and FPZ can be significant and, at times, comparable. Irrespective of the material and size-effect, samples that are sufficiently large ($D \gg r_p$) will undergo fracture-driven failure, while samples with sizes below the characteristic fracture length ($D \leq r_p$) will experience strength-driven failure [1,17,18,35,48,49]. This is illustrated in Fig. 4.

Bažant-type size effect laws, which quantify changes in nominal strength (σ_N) with sample size are used to analyze energetic fracture size-effects. The size-effect law (SEL) was initially developed for quasi-brittle materials where FPZ ≫ PZ [17]. More recently, Nguyen et al. [46] have developed a model for materials whose PZ ≫ FPZ, which as a first approximation, is more representative of the materials studied here. This SEL law is expressed as:

$$\sigma_N = \frac{\sigma_o}{\sqrt{1 + D/D_o}}, \tag{1}$$

where

$$\sigma_o = \sqrt{E^* G_t / 2r_p}, \text{ and } D_0 = 2r_p / g(\alpha_0). \tag{2}$$

Here, σ_o is the maximum material strength, E^* is the effective Young's modulus, G_t is the total fracture energy, $g(\alpha_o)$ is the dimensionless energy release rate, r_p is the size of the yielding zone, and D_o is the characteristic fracture length scale [46,50]. In the limits of this model, materials with small dimensions ($D \ll D_o$) will experience strength-governed failure with $\sigma_N \propto D$, while materials with large dimensions ($D \gg D_o$) will experience fracture-driven failure with $\sigma_N \propto D^{-1/2}$. Despite the extensive work in this area, there is still a need for better theoretical frameworks when FPZ ~ PZ. More importantly, it is crucial to characterize the relative process zone sizes to understand the underlying causes of ductile to brittle transitions.

4.1. Yielding zone estimation

We first assess the size of the yielding zone using a simple LEFM approximation of $r_p = \frac{1}{2\pi}\frac{G_t E^*}{\sigma_y^2}$, where σ_y is the yield strength. It should be noted that this is a generalized expression that does not account for the plastic hardening or the geometry of the structure, both of which can significantly impact the plastic zone [51,52]. Using the approximate fracture energy dissipation J_Q measured in this study and yield strength values from literature [27,28], we estimate r_p values of ~60 μm, 13 μm, and 6 μm for DC_{17}, DC_{27} and DC_{80}, respectively, where, e.g., DC_{17} is a DC of 17%. It is apparent that changes in cross-linking cause a significant change in process zone size, with r_p decreasing by ~10× as DC changes from 20%–80%. The r_p values are illustrated with respect to the beam dimensions in Fig. 3A.

4.2. SEL analysis

An SEL analysis was used to obtain a more precise experimental yielding zone size by taking specimens of varying sizes and analyzing changes in their nominal strength with sample size, as described by Eqs. (1) and (2). Three geometrically scaled DC_{27} and DC_{80} samples with beam thicknesses of 8.5 μm, 17 μm and 26 μm were tested to failure, and their load–displacement data was analyzed using the SEL-based linear regression method to determine G_t and r_p [46]. Details of the calculations can be found in Supplementary Materials (Fig. S4). DC_{17} samples were excluded because the estimated r_p is larger than what could realistically be made using TPL-DLW, meaning the SEL analysis would be invalid. G_t values of ~ 68 J/m^2 and ~ 55 J/m^2 and r_p values of 8 μm and 2 μm were obtained for DC_{27} and DC_{80}, respectively. These results demonstrate that the r_p size is reduced by a factor of ~4× as DC increases from 27% to 80%, and importantly that the r_p for the DC_{27} specimens begins to approach the 26 μm sample thickness.

4.3. Numerical quantification of r_p and l_{ch}

An elastic–plastic-damage FE model [34] was implemented to more thoroughly investigate the yielding zone size and shape, along with the relative sizes of the constituent FPZ and PZ with changing DC. Model properties were fit directly from experimental data, and full details of the model setup are provided in *Materials and Methods* and in the Supplementary Materials. This model allows an estimate of the maximum possible FPZ and PZ size, as well as the fracture energy due to damage (G_f).

In this model, the process zones are considered to be fully developed when (i) the first element at the crack tip reaches a stress-free state and (ii) the stress gradient does not change as the crack propagates. The crack normal stress (σ_{xx}) at this instant is plotted against the distance from the crack tip in Fig. 5. The value of l_{ch} is taken to be the distance from the crack tip to the point of maximum stress or fracture stress ($\sigma_{fracture}$). In DC_{27} and DC_{80} samples, the l_{ch} values are found to be 2.4 μm and 1.0 μm respectively. In the DC_{17} samples, the small sample size did not allow the FPZ to fully develop, as indicated by the non-zero stress at the tip of the crack (Fig. 5D). To determine l_{ch}, a 120×

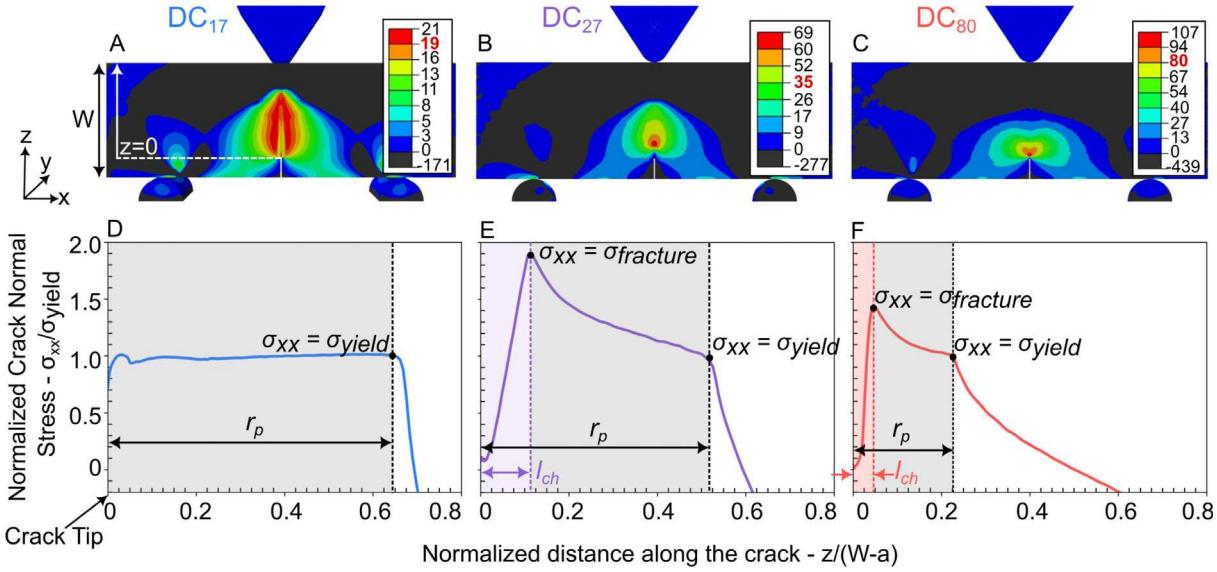

Fig. 5. Numerical modeling of FPZ and PZ A, B, C: Crack normal stress (σ_{xx}) distribution in the mid-plane of DC_{17}, DC_{27} and DC_{80} W = 26 μm beams, after the yielding zone is fully developed. The bold-red value in the scale bar indicates the yield strength. D, E, F: Crack normal stress normalized by yield strength as a function of distance from the crack tip normalized by length (W-a) for DC_{17}, DC_{27} and DC_{80} beams, respectively. The plots highlight the yielding zone (r_p) and the relative size of the FPZ (l_{ch}). (For interpretation of the references to color in this figure legend, the reader is referred to the web version of this article.)

Table 1
Total fracture energy (G_t), damage fracture energy (G_f), plastic fracture energy (G_p), FPZ (l_{ch}) and yielding zone (r_p) for different degrees of conversion (DC).

DC	G_t (J/m^2)	G_f (J/m^2)	G_p (J/m^2)	l_{ch} (μm)	r_p (μm)
17	–	90	–	115	280
27	68	28	40	2.4	11
80	55	18	37	1.0	5

scaled-up version of the beam was modeled, revealing an FPZ size of 115 μm (Fig. S6).

The PZ size is taken to be the distance from the peak stress in front of the crack tip (i.e., the end of the FPZ) to the point where $\sigma_{xx} = \sigma_y$ (Fig. 5). In the 26 μm thick beams, plastic zones were found to have a considerable size of 14 μm, 11 μm, and 5 μm for the DC_{17}, DC_{27}, and DC_{80} samples, respectively. It should be noted that the PZ was not fully developed for the DC_{17} sample here, and in 120× scaled simulations for the DC_{17} beam, the fully developed PZ size is found to be 165 μm.

These results provide critical insight into how fracture behaviors change according to FPZ and PZ size. As the DC decreases from 80% to 17%, the FPZ and PZ size increase by ~115× and ~33×, respectively. This substantial size increase is most prominent in the DC_{low} specimens, and the change is more modest between the DC_{med} and DC_{high} specimens. These trends align with observed variations in strength and bending stiffness, which show a similarly steep increase in the DC_{low} regime (Fig. 3). Importantly, these results demonstrate that for the DC_{17} beams, both the FPZ and PZ are significantly larger than the 26 μm experimental sample thickness. This indicates that the observed ductility in the DC_{low} specimens is the result of an underdeveloped yielding zone that does not meet the G_t required to cause fracture.

4.4. Damage and plasticity governed fracture

The relative contributions of the FPZ and PZ in the fracture of beams with varying DC can be further characterized by comparing the damage and plastic energy dissipation rate, G_f and G_p, respectively. The plastic energy dissipation rate G_p was determined by subtracting the damage fracture energy G_f obtained from the FE model from the total fracture energy G_t determined from the SEL experiments (i.e., $G_p = G_t - G_f$), the results from which are shown in Table 1. We find that in the DC_{80} specimens, the plastic energy dissipation rate (G_p = 37 J/m^2) contributes ~2× that of the energy dissipated via damage (G_f = 18 J/m^2), despite exhibiting very brittle failure. In comparison, despite an almost comparable plastic energy dissipation rate (G_p = 40 J/m^2), the DC_{27} specimens have a slightly higher total fracture energy, mainly due to an increase in the damage energy dissipation (G_f = 28 J/m^2). The DC_{17} specimens have a very high damage energy dissipation of G_f = 90 J/m^2, and likely have an even higher G_p, but it was not possible to estimate this value because SEL experiments were not conducted on these specimens. These relative changes in plastic and damage energy dissipation correlate well with the increased r_p and l_{ch} for lower DC samples.

It is interesting to note that the PZ size is larger than the FPZ size across all the DC values examined in this work. This, along with the consistent trend of $G_p > G_f$ for all the samples, indicates that the fracture behavior is more affected by plasticity than damage. However, this difference is not substantial enough to cause a purely ductile fracture at small scales, as illustrated in Fig. 5. The fracture behavior of these photopolymers thus falls in an intermediate regime, where both softening and hardening ahead of the crack tip impact crack growth, warranting further analysis to understand the emergent size-affected behavior. This also suggests that the r_p and G_t values calculated using the SEL law in Eqs. (1) and (2) in Section 4.2 might not be fully accurate and there is a need for improved SEL models for this intermediate regime that can capture this behavior more comprehensively.

Lastly, we note that the yielding zone sizes determined from the numerical model are comparable to the estimates obtained from the LEFM model for the DC_{med} and DC_{high} specimens, but the DC_{low} LEFM estimate significantly underestimated the actual r_p size. This result is unsurprising given that the J_Q value obtained from the experiments is an underestimate of the actual G_t, but that the DC_{med} and DC_{high} specimens had a nearly fully developed r_p. The LEFM estimate nevertheless provided a quick and useful estimation of the characteristic material length scale that would be useful for predicting size-affected changes in properties.

4.5. Size-affected ductility

To comprehensively understand the effect of changing both polymer composition and size, we evaluate the change in sample strength (σ_N)

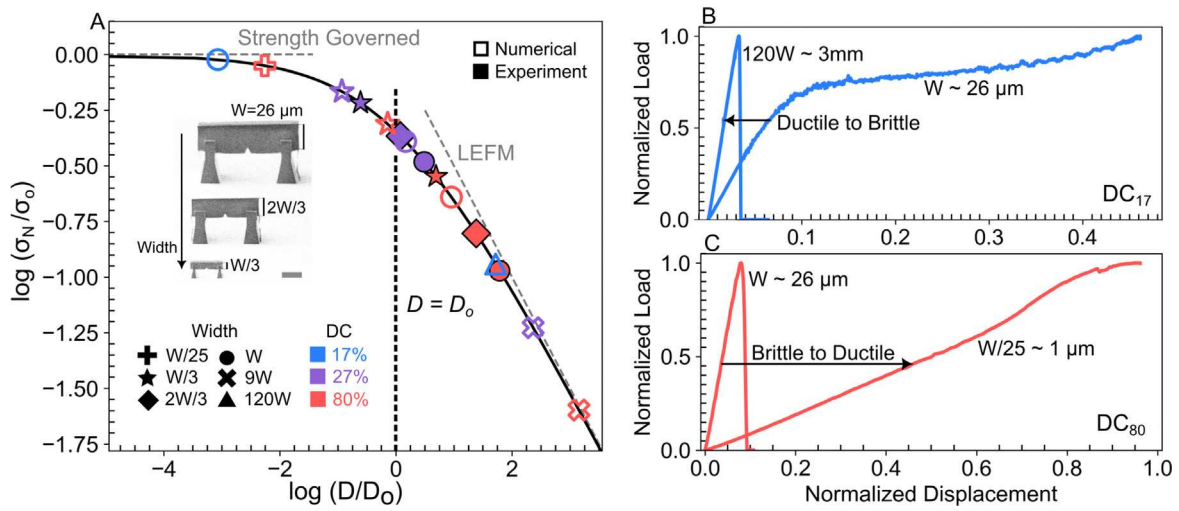

Fig. 6. LEFM vs. strength governed failure. (A) A SEL plot of nominal strength (σ_N) normalized by material strength (σ_o) vs. sample dimension (D) normalized by the transition fracture length (D_o). Experimental and numerical results are shown for different sample sizes and degrees of conversion. Scale bar: 10 μm. (B) Ductile to Brittle transition in DC_{80} as the sample size is increased from 26 μm to 3 mm. (C) Brittle to Ductile transition in DC_{17} as the sample size is decreased from 26 μm to 1 μm.

with sample size (D) in the context of an SEL analysis. The parameters to calculate the constituent material strength (σ_o) and transition fracture length (D_o) (Eq. (2)), are determined from SEL experiments in combination with numerical models, and normalized SEL data is shown in Fig. 6. For structures of the same size ($D = W = 26$ μm), comparing the sample strength to the material strength (σ_N/σ_o) revealed that decreasing the DC causes a transition from flaw-based to strength-based failure. For the DC_{80} specimens, the yielding zone is significantly smaller than the sample size ($r_p \ll$ D), causing it to fall close to the LEFM-dominated regime of the SEL curve. In the DC_{27} specimens, the yielding zone size approaches the sample size but is still smaller ($r_p \leq$ D), causing an observed transition from LEFM to strength-based fracture. The DC_{17} specimens are significantly smaller than the yielding zone size ($D \gg r_p$), falling well into the strength-governed fracture regime. It is clear from these trends that *ductility emerges when* $D \sim r_p$.

For structures of the same composition, the emergence of ductility at sufficiently small sizes and the emergence of brittleness at sufficiently large sizes was confirmed by further analyzing size effect experiments and doing additional numerical simulations for sizes that were not possible to fabricate experimentally. Experimentally scaled down DC_{80} specimens do not show pronounced ductility, possibly because the smallest possible beam thickness ($W/3 = 8$ μm) was still larger than the r_p of these materials, but they do show a slower crack propagation velocity (Fig. S7). Numerically modeled DC_{80} beams of size $W/25$ (~ 1 μm) exhibit ductility similar to the DC_{17} specimens (Fig. 6). For DC_{17} specimens, a numerically modeled beam of size $120W$ (~ 3 mm) was found to show a characteristic brittle failure, indicating the significantly large r_p of this material. These results illustrate that *irrespective of the constituent material's composition, ductile or brittle fracture behavior can be controlled simply by changing specimen size.*

It should be noted that the slight discrepancy between the experimental and numerical results on the SEL curve results from different methods used to calculate r_p, namely the SEL method for experiments and a direct measurement for the FE models. Although simple size-effect laws developed from quasi-brittle materials (FPZ ≫ PZ) are useful understand the changes in fracture behavior in this study, the need for a full numerical model to quantify fracture energy, FPZ and PZ in these materials highlights the complex interplay between structural dimensions and material properties and reestablishes the need for improved size-effect models for when FPZ~PZ.

5. Summary and perspectives

In this work, we use μSENB experiments and corresponding FE modeling to study the fracture behavior and process zone sizes of a TPL-DLW polymer as a function of DC and part size. While increasing the DC from 17% to 80% increases both strength and stiffness by ~3× and ~4×, respectively, there is a corresponding ~6× reduction in toughness and a corresponding DBT in the failure behavior. Experiments on differently sized beams in combination with an elastic–plastic-damage FE model reveal significant changes in fracture energy and yield zone size r_p, which change by nearly two orders of magnitude across the DC range studied here. Despite this variation, the relative sizes of the FPZ and PZ were comparable, indicating that the observed fracture behavior falls in an intermediate range between ductile and quasi-brittle fracture. By analyzing the specimens in the context of a SEL framework, it becomes apparent that ductility emerges when the sample size approaches the yielding zone size ($D \approx r_p$) and additionally corresponds with a transition from flaw-governed to strength-governed failure. These results demonstrate that ductility is an emergent property even in traditionally brittle materials and that process parameters and feature size are both crucial factors in creating materials with enhanced mechanical properties.

Understanding characteristic fracture lengths is thus crucial for designing any component where mechanical performance is a priority. For instance, tougher engineering composites can be created by controlling the fiber spacing or fiber diameter in a reinforced composite. This work has long-term applications in sustainable materials development, wherein earth-abundant materials that are thought to be intrinsically brittle, like silica, can be made ductile and used in tough composites, much like what is found in natural materials. Processing or compositional changes such as heating, filler addition, or grain size modification inevitably alter process zone sizes and can drastically alter fracture behaviors. By characterizing fracture size effects, ductile to brittle transitions can be accounted for in such materials, and feature sizes in components can be controlled to prevent catastrophic failure. In the context of additively manufactured materials, there is a new potential to design feature sizes to match constituent characteristic length scales and maximize toughness while maintaining strength and stiffness. Moreover, the strength and stiffness of a structure can be controlled by altering the material composition, while the fracture behavior can be modified by adjusting the feature sizes within the architecture.

In the case of parts produced using TPL, the typical feature sizes of 200 nm–5 μm are in the same range as the process zone sizes of many

of the constituents, making it an ideal system for studying size-affected changes in architected material toughness, although it requires the development of better analytical models to quantify fracture size effects in materials with large process zones. Importantly, greater attention needs to be paid to materials with a high *DC*. While thermal treatment has been suggested as a solution to property variation between prints [28], the resulting small process zone leads to more brittle behaviors, as is likely the case in materials that have inadvertently been thermally annealed during atomic layer deposition or plasma etching [53,54]. Considering the role of feature size on ductility in any additive manufacturing material can offer enhanced tunability in structural design. It additionally becomes possible to cascade multiple damage mechanisms in hierarchical architectures to develop highly tough and damage-tolerant materials, as is commonly seen in many natural structural materials [55].

CRediT authorship contribution statement

Zainab S. Patel: Writing – review & editing, Writing – original draft, Visualization, Validation, Methodology, Investigation, Formal analysis, Conceptualization. **Abdulaziz O. Alrashed:** Investigation. **Kush Dwivedi:** Writing – review & editing, Visualization, Investigation, Formal analysis. **Marco Salviato:** Writing – review & editing, Supervision, Methodology, Investigation, Formal analysis. **Lucas R. Meza:** Methodology, Conceptualization, Supervision, Writing – original draft, Writing – review & editing.

Declaration of competing interest

The authors declare the following financial interests/personal relationships which may be considered as potential competing interests: Lucas Meza reports financial support was provided by National science Foundation. If there are other authors, they declare that they have no known competing financial interests or personal relationships that could have appeared to influence the work reported in this paper.

Data availability

All the data in this study is included in the main manuscript and/or supplementary.

Acknowledgments

The authors gratefully acknowledge the financial support from the National Science Foundation, United States under the Mechanics of Materials and Structures program managed by S. Qidwai (award no. 2032539). Part of this work was conducted at the Washington Nanofabrication Facility and Molecular Analysis Facility, a National Nanotechnology Coordinated Infrastructure (NNCI) site at the University of Washington, with partial support from the National Science Foundation, United States via awards NNCI-1542101 and NNCI-2025489.

Appendix A. Supplementary data

Supplementary material related to this article can be found online at https://doi.org/10.1016/j.addma.2024.104113.

References

[1] Johannes Ast, Matteo Ghidelli, Karsten Durst, Mathias Göken, Marco Sebastiani, Alexander M. Korsunsky, A review of experimental approaches to fracture toughness evaluation at the micro-scale, Mater. Des. 173 (2019) 107762.
[2] Souheng Wu, Control of intrinsic brittleness and toughness of polymers and blends by chemical structure: A review, Polym. Int. 29 (3) (1992) 229–247.
[3] Q.Q. Duan, R.T. Qu, P. Zhang, Z.J. Zhang, Z.F. Zhang, Intrinsic impact toughness of relatively high strength alloys, Acta Mater. 142 (2018) 226–235.
[4] Fei Xie, Qingjun Chen, Jiwen Gao, Brittle–ductile transition in laser 3D printing of Fe-based bulk metallic glass composites, Metals 9 (1) (2019) 78.
[5] Anar Nurizada, Kedar Kirane, Induced anisotropy in the fracturing behavior of 3D printed parts analyzed by the size effect method, Eng. Fract. Mech. 239 (2020) 107304.
[6] Luca Quagliato, Soo Yeon Kim, Seok Chang Ryu, Quasi-ductile to brittle transitional behavior and material properties gradient for additively manufactured SLA acrylate, Mater. Lett. 329 (2022) 133121.
[7] Shanshan Xu, Jean-Francois Tahon, Isabelle De-Waele, Grégory Stoclet, Valerie Gaucher, Brittle-to-ductile transition of PLA induced by macromolecular orientation, eXPRESS Polym. Lett. 14 (11) (2020) 1037–1047.
[8] Tomas F. Babuska, Mark A. Wilson, Kyle L. Johnson, Shaun R. Whetten, John F. Curry, Jeffrey M. Rodelas, Cooper Atkinson, Ping Lu, Michael Chandross, Brandon A Krick, et al., Achieving high strength and ductility in traditionally brittle soft magnetic intermetallics via additive manufacturing, Acta Mater. 180 (2019) 149–157.
[9] Peter Bernhard Hirsch, S.G. Roberts, J. Samuels, The brittle–ductile transition in silicon. II. Interpretation, Proc. R. Soc. Lond. Ser. A Math. Phys. Eng. Sci. 421 (1860) (1989) 25–53.
[10] Fredrik Östlund, Karolina Rzepiejewska-Malyska, Klaus Leifer, Lucas M. Hale, Yuye Tang, Roberto Ballarini, William W. Gerberich, Johann Michler, Brittle-to-ductile transition in uniaxial compression of silicon pillars at room temperature, Adv. Funct. Mater. 19 (15) (2009) 2439–2444.
[11] Inas Issa, Christoph Gammer, Stefan Kolitsch, Anton Hohenwarter, Peter J. Imrich, Reinhard Pippan, Daniel Kiener, In-situ TEM investigation of toughening in silicon at small scales, Mater. Today 48 (2021) 29–37.
[12] Almut Albiez, Ruth Schwaiger, Size effect on the strength and deformation behavior of glassy carbon nanopillars, MRS Adv. 4 (2) (2019) 133–138.
[13] Xuan Zhang, Lei Zhong, Arturo Mateos, Akira Kudo, Andrey Vyatskikh, Huajian Gao, Julia R. Greer, Xiaoyan Li, Theoretical strength and rubber-like behaviour in micro-sized pyrolytic carbon, Nature Nanotechnol. 14 (8) (2019) 762–769.
[14] Dahye Shin, Dongchan Jang, Crack-tip plasticity and intrinsic toughening in nano-sized brittle amorphous carbon, Int. J. Plast. 127 (2020) 102642.
[15] David Z. Chen, X.W. Gu, Qi An, W.A. Goddard, Julia R. Greer, Ductility and work hardening in nano-sized metallic glasses, Appl. Phys. Lett. 106 (6) (2015).
[16] Yu Zou, Pawel Kuczera, Alla Sologubenko, Takashi Sumigawa, Takayuki Kitamura, Walter Steurer, Ralph Spolenak, Superior room-temperature ductility of typically brittle quasicrystals at small sizes, Nature Commun. 7 (1) (2016) 12261.
[17] Zdenek P. Bažant, Size effect in blunt fracture: Concrete, rock, metal, J. Eng. Mech. 110 (4) (1984) 518–535.
[18] Zdenek P. Bažant, Mohammad T. Kazemi, Size effect in fracture of ceramics and its use to determine fracture energy and effective process zone length, J. Am. Ceram. Soc. 73 (7) (1990) 1841–1853.
[19] Zdenek P. Bazant, Size effect on structural strength: A review, Arch. Appl. Mech. 69 (1999) 703–725.
[20] Zdenek P. Bažant, Jia-Liang Le, Marco Salviato, Quasibrittle Fracture Mechanics and Size Effect: A First Course, Oxford University Press, 2021.
[21] Shoji Maruo, Osamu Nakamura, Satoshi Kawata, Three-dimensional microfabrication with two-photon-absorbed photopolymerization, Opt. Lett. 22 (2) (1997) 132–134.
[22] Kwang-Sup Lee, Ran Hee Kim, Dong-Yol Yang, Sang Hu Park, Advances in 3D nano/microfabrication using two-photon initiated polymerization, Prog. Polym. Sci. 33 (6) (2008) 631–681.
[23] Lucas R. Meza, Satyajit Das, Julia R. Greer, Strong, lightweight, and recoverable three-dimensional ceramic nanolattices, Science 345 (6202) (2014) 1322–1326.
[24] Jens Bauer, Almut Schroer, Ruth Schwaiger, Oliver Kraft, Approaching theoretical strength in glassy carbon nanolattices, Nature Mater. 15 (4) (2016) 438–443.
[25] Jens Bauer, Lucas R. Meza, Tobias A. Schaedler, Ruth Schwaiger, Xiaoyu Zheng, Lorenzo Valdevit, Nanolattices: An emerging class of mechanical metamaterials, Adv. Mater. 29 (40) (2017) 1701850.
[26] Xiaoxing Xia, Christopher M. Spadaccini, Julia R. Greer, Responsive materials architected in space and time, Nat. Rev. Mater. 7 (9) (2022) 683–701.
[27] Jens Bauer, Anna Guell Izard, Yunfei Zhang, Tommaso Baldacchini, Lorenzo Valdevit, Programmable mechanical properties of two-photon polymerized materials: From nanowires to bulk, Adv. Mater. Technol. 4 (9) (2019) 1900146.
[28] Jens Bauer, Anna Guell Izard, Yunfei Zhang, Tommaso Baldacchini, Lorenzo Valdevit, Thermal post-curing as an efficient strategy to eliminate process parameter sensitivity in the mechanical properties of two-photon polymerized materials, Opt. Express 28 (14) (2020) 20362–20371.
[29] ASTM E1820-18, Standard Test Method for Measurement of Fracture Toughness, Technical Report, ASTM International, 2011.
[30] Zainab S. Patel, Lucas R. Meza, Toughness amplification via controlled nanostructure in lightweight nano-bouligand materials, Small 2207779 (2023).
[31] Andrew J. Gross, Katia Bertoldi, Additive manufacturing of nanostructures that are delicate, complex, and smaller than ever, Small 15 (33) (2019) 1902370.
[32] Tommaso Baldacchini, Maxwell Zimmerley, Chun-Hung Kuo, Eric O. Potma, Ruben Zadoyan, Characterization of microstructures fabricated by two-photon polymerization using coherent anti-stokes Raman scattering microscopy, J. Phys. Chem. B 113 (38) (2009) 12663–12668.
[33] Fahmy M. Haggag, John H. Underwood, Compliance of a Three-point Bend Specimen at Load Line, Technical Report, Army armament research and development center Watervliet NY Large caliber, 1984.

[34] Marco Salviato, Adding multi-material regions embracing the tip leads to significant capacity increase in structures weakened by V-notches under antiplane shear and torsion, Int. J. Solids Struct. 250 (2022) 111704.
[35] Yao Qiao, Marco Salviato, Strength and cohesive behavior of thermoset polymers at the microscale: A size-effect study, Eng. Fract. Mech. 213 (2019) 100–117.
[36] Yao Qiao, Marco Salviato, Micro-computed tomography analysis of damage in notched composite laminates under multi-axial fatigue, Composites B 187 (2020) 107789.
[37] Robert O. Ritchie, The conflicts between strength and toughness, Nature Mater. 10 (11) (2011) 817–822.
[38] G.J. Lake, A.G. Thomas, The strength of highly elastic materials, Proc. R. Soc. A 300 (1460) (1967) 108–119.
[39] S.N. Zhurkov, V.E. Korsukov, Atomic mechanism of fracture of solid polymers, J. Polym. Sci. Polym. Phys. Ed. 12 (2) (1974) 385–398.
[40] Shi-Qing Wang, Shiwang Cheng, Panpan Lin, Xiaoxiao Li, A phenomenological molecular model for yielding and brittle–ductile transition of polymer glasses, J. Chem. Phys. 141 (9) (2014) 094905.
[41] Aaliyah Z. Dookhith, Nathaniel A. Lynd, Gabriel E. Sanoja, Tailoring rate and temperature-dependent fracture of polyether networks with organoaluminum catalysts, Macromolecules 56 (1) (2022) 40–48.
[42] Akash Arora, Tzyy-Shyang Lin, Haley K. Beech, Hidenobu Mochigase, Rui Wang, Bradley D. Olsen, Fracture of polymer networks containing topological defects, Macromolecules 53 (17) (2020) 7346–7355.
[43] Shaoting Lin, Jiahua Ni, Dongchang Zheng, Xuanhe Zhao, Fracture and fatigue of ideal polymer networks, Extreme Mech. Lett. 48 (2021) 101399.
[44] H.R. Brown, A model for brittle–ductile transitions in polymers, J. Mater. Sci. 17 (1982) 469–476.
[45] A.S. Argon, R.E. Cohen, Toughenability of polymers, Polymer 44 (19) (2003) 6013–6032.
[46] Hoang T. Nguyen, A. Abdullah Dönmez, Zdeněk P. Bažant, Structural strength scaling law for fracture of plastic-hardening metals and testing of fracture properties, Extreme Mech. Lett. 43 (2021) 101141.
[47] Cory Hage Mefford, Yao Qiao, Marco Salviato, Failure behavior and scaling of graphene nanocomposites, Compos. Struct. 176 (2017) 961–972.
[48] Zdenek P. Bazant, Size effect, Int. J. Solids Struct. 37 (1–2) (2000) 69–80.
[49] Zdenek P. Bazant, M.T. Kazemi, Determination of fracture energy, process zone length and brittleness number from size effect, with application to rock and concrete, Int. J. Fract. 44 (1990) 111–131.
[50] G.V. Guinea, J.Y. Pastor, J. Planas, M. Elices, Stress intensity factor, compliance and CMOD for a general three-point-bend beam, Int. J. Fract. 89 (1998) 103–116.
[51] S.K. Kudari, B. Maiti, K.K. Ray, The effect of specimen geometry on plastic zone size: A study using the j integral, J. Strain Anal. Eng. Des. 42 (3) (2007) 125–136.
[52] Ghennadiy Vsevolodovich Klevtsov, Ludmila Rafailovna Botvina, Natal'ya Arturovna Klevtsova, Plastic zones formation under different types of loading conditions, ISIJ Int. 36 (2) (1996) 215–221.
[53] Lucas R. Meza, Alex J. Zelhofer, Nigel Clarke, Arturo J. Mateos, Dennis M. Kochmann, Julia R. Greer, Resilient 3D hierarchical architected metamaterials, Proc. Natl. Acad. Sci. 112 (37) (2015) 11502–11507.
[54] Widianto P. Moestopo, Sammy Shaker, Weiting Deng, Julia R. Greer, Knots are not for naught: Design, properties, and topology of hierarchical intertwined microarchitected materials, Sci. Adv. 9 (10) (2023) 6725.
[55] Wei Huang, David Restrepo, Jae-Young Jung, Frances Y. Su, Zengqian Liu, Robert O. Ritchie, Joanna McKittrick, Pablo Zavattieri, David Kisailus, Multiscale toughening mechanisms in biological materials and bioinspired designs, Adv. Mater. 31 (43) (2019) 1901561.